Single nanoparticle detection using split-mode microcavity Raman lasers

Bei-Bei Li[a], William R. Clements[a], Xiao-Chong Yu[a], Kebin Shi[a,b], Qihuang Gong[a,b], and Yun-Feng Xiao[a,b,1]

[a]State Key Laboratory for Mesoscopic Physics and School of Physics, Peking University, Beijing 100871, China; and [b]Collaborative Innovation Center of Quantum Matter, Beijing 100871, China

Edited by Oskar J. Painter, California Institute of Technology, Pasadena, CA, and accepted by the Editorial Board September 9, 2014 (received for review May 7, 2014)

Ultrasensitive nanoparticle detection holds great potential for early-stage diagnosis of human diseases and for environmental monitoring. In this work, we report for the first time, to our knowledge, single nanoparticle detection by monitoring the beat frequency of split-mode Raman lasers in high-Q optical microcavities. We first demonstrate this method by controllably transferring single 50-nm–radius nanoparticles to and from the cavity surface using a fiber taper. We then realize real-time detection of single nanoparticles in an aqueous environment, with a record low detection limit of 20 nm in radius, without using additional techniques for laser noise suppression. Because Raman scattering occurs in most materials under practically any pump wavelength, this Raman laser-based sensing method not only removes the need for doping the microcavity with a gain medium but also loosens the requirement of specific wavelength bands for the pump lasers, thus representing a significant step toward practical microlaser sensors.

stimulated Raman scattering | optical microcavity | mode splitting | optical sensor | label free

Stimulated Raman scattering holds great potential for various photonic applications, such as label-free high-sensitivity biomedical imaging (1) and for extending the wavelength range of existing lasers (2), as well as for generating ultra-short light pulses (3). In high Q microcavities (4), stimulated Raman scattering, also called Raman lasing, has been experimentally demonstrated to possess ultra-low thresholds (5–12), due to the greatly increased light density in microcavities (13). Such microcavity Raman lasers hold great potential for sensing applications. In principle, Raman lasing initially occurs in the two initially degenerate counter propagating traveling cavity modes. These two modes couple to each other due to backscattering when a nanoscale object binds to the cavity surface. For a sufficiently strong coupling, in which the photon exchange rate between the two initial modes becomes larger than the rates of all of the loss mechanisms in the system, two new split cavity modes form (14–18) and lase simultaneously. Thus, by monitoring the beat frequency of the split-mode Raman lasers, ultrasensitive nanoparticle detection can be realized.

In this work, we report, to our knowledge, the first experimental demonstration of single nanoparticle detection using split-mode microcavity Raman lasers. The sensing principle is first demonstrated in air, by controllably binding or removing single 50-nm-radius polystyrene (PS) nanoparticles to and from the cavity surface using a fiber taper (19) and measuring the changes in the beat frequency of the two split Raman lasers. Real-time single nanoparticle detection is then performed in an aqueous environment by monitoring the discrete changes in beat frequency of the Raman lasers, and a detection limit of 20 nm in particle radius is realized. This microcavity Raman laser sensing method holds several advantages. On the one hand, the beat frequency of the Raman lasers, which corresponds to the mode splitting (18), is inherently immune to many noise sources, such as laser frequency noise and thermal noise (including that induced both by the environmental temperature fluctuations and by probe laser heating), which are the main noise sources in sensing systems using the mode shift mechanism (20–30). Over the last few years, significant effort has been made to suppress the laser frequency noise in the mode-shift detection method, such as by using a reference interferometer (27) and by performing backscattering detection with frequency locking techniques (28, 29), but both approaches involve a substantial increase in the complexity of the sensing systems. On the other hand, the intrinsic Raman gain in the cavity provides a perfect means to compensate for the cavity mode loss and thus to lower the detection limit compared with passive mode splitting methods (18, 31–34). Without the need for doping the microcavities with a gain medium (35–37), the fabrication complexity of microcavities is also greatly reduced, and no specific wavelength bands of the pump lasers are required.

Results

Characterization of the Microcavity Raman Lasers. A schematic of the measurement system is shown in Fig. 1*A*. A tunable pump laser in the 680-nm wavelength band is used to generate stimulated Raman scattering in a silica microcavity in both air and aqueous environments. To demonstrate the sensing mechanism for the control experiment in air, we use microtoroids on a silicon wafer (38), with major (minor) diameters of ~50 (6) μm. A fiber taper (39) with a diameter of ~500 nm is used to couple the pump light into the whispering gallery modes (WGMs) of the microcavity and to collect the output. Stimulated Raman scattering in the silica occurs when enough pump photons propagate in the cavity. The normalized Raman gain spectrum of bulk silica (40) is plotted in Fig. 1*B*. The *Inset* is a close-up to the section of maximum Raman gain at which cavity Raman lasing occurs (~13 THz or 433 cm^{-1}), with R+ and R− denoting the two split Raman cavity modes. In our experiment, the wavelength of the pump light is scanned through a pump cavity mode ($Q \sim 4 \times 10^7$), and the output light is divided into three ports to measure the transmission spectrum (Fig. 1*C*), the Raman spectrum (Fig. 1*D*, with a threshold of ~350 μW plotted in the *Inset*), and the Raman power in the

Significance

Optical sensing with ultrahigh sensitivity of single nanoscale objects is strongly desirable for applications in various fields, such as in early-stage diagnosis of human diseases and in environmental monitoring, as well as in homeland security. In this article, we report an optical technique for single nanoparticle detection in both air and an aqueous environment, with an ultralow detection limit.

Author contributions: Y.F.X. conceived the idea, designed the experiment, and supervised the project; B.B.L. performed the experiment; W.R.C. contributed to the theoretical work; B.B.L., X.C.Y., and Y.F.X. analyzed the data; and B.-B.L., W.R.C., X.-C.Y., K.S., Q.G., and Y.-F.X. contributed to the discussion and wrote the paper.

The authors declare no conflict of interest.

This article is a PNAS Direct Submission. O.J.P. is a guest editor invited by the Editorial Board.

[1]To whom correspondence should be addressed. Email: yfxiao@pku.edu.cn.

This article contains supporting information online at www.pnas.org/lookup/suppl/doi:10.1073/pnas.1408453111/-/DCSupplemental.

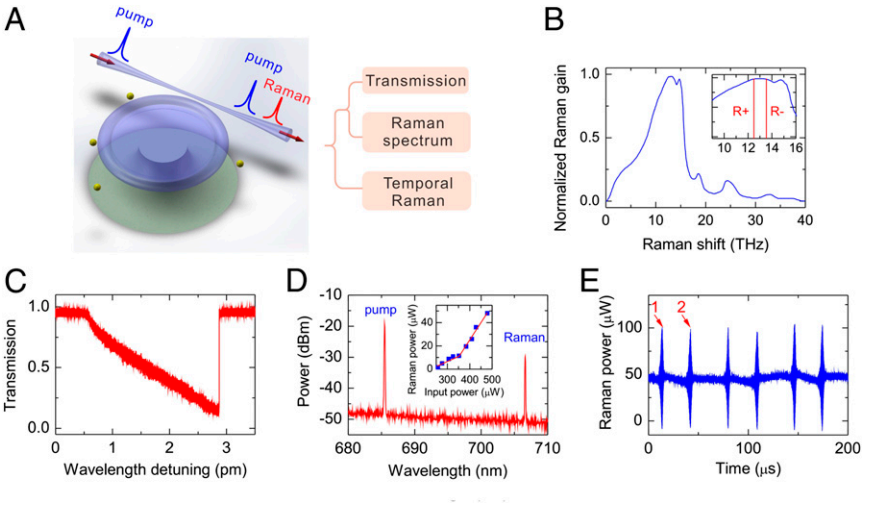

Fig. 1. Measurement system for the microcavity Raman laser. (*A*) Schematic illustration of the taper-toroid coupling system. The output light containing both the pump and Raman lasers is divided into three ports to measure the pump transmission spectrum (*C*), Raman spectrum (*D*), and Raman power in the time domain (*E*). (*B*) Normalized Raman gain spectrum of bulk silica. (*Inset*) Close-up to the section of maximum Raman gain, with R+ and R− representing the two split Raman cavity modes. In the temporal Raman port, a band-pass filter with a center wavelength of 710 nm and a bandwidth of 10 nm is used to block the pump laser. (*C*) Transmission spectrum of the pump cavity mode during the wavelength up-scan. The spectrum experiences a significant line width broadening compared with the original resonance, because the pump light pushes the cavity resonance to longer wavelength due to the thermal effect. (*D*) The first-order Raman spectrum. (*E*) The Raman power in the time domain, which exhibits periodic envelopes with the first two marked by 1 and 2, respectively.

time domain (Fig. 1*E*). In the temporal Raman port, we use a band-pass filter (center wavelength: ∼710 nm, bandwidth: ∼10 nm) to block the pump laser and collect only the first-order Raman laser light.

Under a 1-mW pump power, the resonance of the pump cavity mode in the transmission spectrum (Fig. 1*C*) exhibits a large broadening during the wavelength up-scan due to thermal effects (41). Furthermore, under the effect of the pump scanning (speed: ∼5.4 nm/s), periodic pairs of envelopes containing fast oscillations (e.g., one typical pair of envelopes 1 and 2, marked in Fig. 1*E*) emerge in the Raman emission in the time domain, with a period of ∼66 μs and a duration time for each envelope of 5 ∼ 6 μs.

Sensing Signal of the Split-Mode Microcavity Raman Lasers. A close-up view of the envelopes in Fig. 1*E* reveals that the envelopes are made up of fast oscillations with a frequency of several tens of megahertz, as shown in Fig. 2*A*, which is a close-up view of envelope 1 marked in Fig. 1*E*. The beat frequency of this oscillation corresponds to the value of the frequency splitting of the two split Raman cavity modes. The beat frequency either monotonously increases or decreases during each envelope (for details, see Fig. S1). The physics for this behavior has been studied and can be briefly explained as follows (for details, see *SI Text*). Generally, the two split Raman modes have different thresholds, and stimulated Raman scattering only occurs in the split Raman mode with the lower threshold due to the clamping effect of the intracavity pump power (40) and strong mode competition. The scanning of the pump wavelength, however, induces periodic hopping between the two split Raman modes. During the hop, both modes lase simultaneously, producing a beat oscillation, corresponding to the observed fast oscillations inside each envelope. The variation of the beat frequency originates from the optical Kerr effect associated with the Raman lasers, which unequally shifts the resonance frequencies of the split modes, due to the different Raman powers in the two modes.

In principle, the moment in which the amplitude of the beat oscillation is largest, at the center of the envelopes (e.g., in red rectangle in Fig. 2*A*, with a close-up displayed in Fig. 2*B*), corresponds to the Raman lasers in the two split modes having the same power. In this case, the beat frequency is equal to the original mode splitting without the influence of the Kerr effect. Experimentally, we find that, independently of whether the oscillations speed up or slow down inside one envelope, the beat frequency in the center part remains unchanged for different envelopes, with the result shown in Fig. 2*C*. In the following sensing experiment, we take the average value of the beat frequencies in all envelopes as the sensing signal.

Temporal Stability of the Sensing Signal. We then measure the temporal stability of the sensing signal defined above. For three

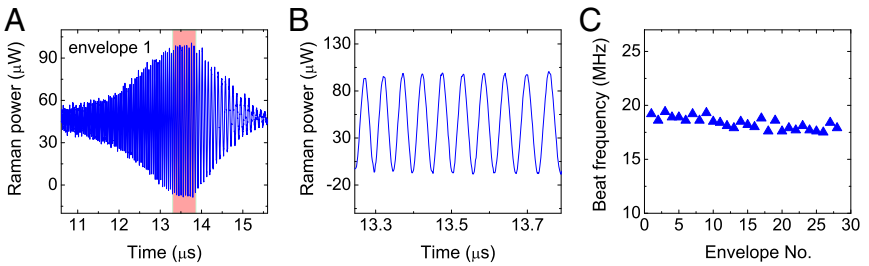

Fig. 2. Sensing signal in the split-mode Raman lasers. (*A*) Close-up of the Raman power in envelope 1 marked in Fig. 1*E*. (*B*) Close-up of the Raman power in the highlighted section of envelope 1 in *A*. (*C*) The beat frequency in the center part of each envelope where the oscillations have the largest amplitude.

different modes A, B, and C, with intrinsic Raman beat frequencies of ~18 (the mode in Figs. 1 and 2), 40, and 53 MHz, we record the average beat frequencies obtained from all envelopes continuously for 30 s with a time interval of 1 s. The results are plotted in Fig. 3, from which we can see that, for all three modes, the average beat frequencies remain stable, with SDs of ~330, ~490, and ~558 kHz during 30 s. In the following control experiment in air, we use the beat frequency of mode A as the sensing signal.

Single Nanoparticle Response in Air. To confirm that this beat frequency does correspond to the splitting of the Raman modes, we first measure the beat frequency with and without a single PS nanoparticle with a radius $r = 50$ nm on the microcavity surface, because the nanoparticle can change the backscattering strength of the cavity field, thus altering the frequency splitting (18). We use a fiber taper to transfer a single nanoparticle (19) (*Methods*) to and from the microcavity surface repeatedly, and in the *Inset* of Fig. 4*A*, we give an optical micrograph showing one nanoparticle bound to the cavity edge. After every nanoparticle transfer process, the beat frequency of the Raman laser is measured, with the result displayed in Fig. 4*A*. It can be seen that every time one nanoparticle is transferred to the cavity surface, a change in the beat frequency is observed; once the nanoparticle is off the cavity surface, the beat frequency goes back to its intrinsic value of ~18.2 MHz. Note that the changes in beat frequency are different for each nanoparticle binding event, because the nanoparticles bind to random positions on the cavity surface, leading to different values for the backscattering of the Raman light and thus to different variations in the mode splitting. These results confirm that the beat frequency does correspond to the splitting of the two lasing modes and can be used as the sensing signal for nanoparticle detection.

We then transfer individual nanoparticles to the cavity surface one by one and measure the change in beat frequency on every nanoparticle binding event. The result is displayed in Fig. 4*B*, in which every discrete variation in the beat frequency corresponds to one nanoparticle binding event. Note that the beat frequency either increases or decreases on every newly bound nanoparticle because the backscattering strength of the Raman light is strongly dependent on both the polar position of each nanoparticle that determines the field intensity where the particle is located and the azimuthal distances between every two particles (17, 32, 42), which determine the interparticle propagating phases of the backscattered Raman laser light.

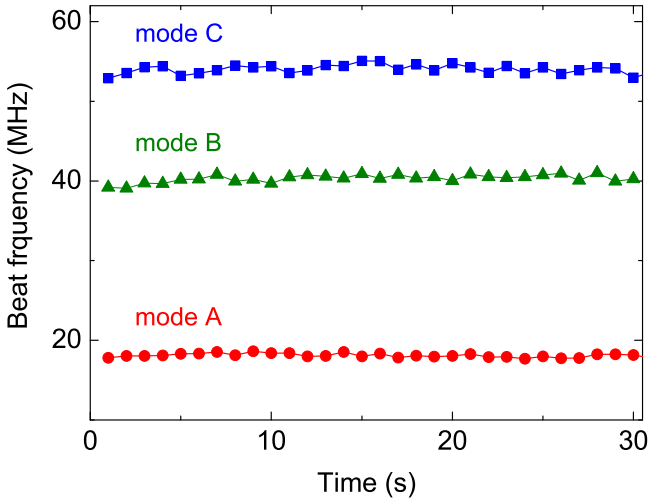

Fig. 3. Measurement of the temporal stability of the beat frequency of the Raman laser. The red circles, olive triangles, and blue squares represent the beat frequencies of three different modes A, B, and C, respectively. The beat frequency of each mode is continuously measured for 30 s with a time interval of 1 s.

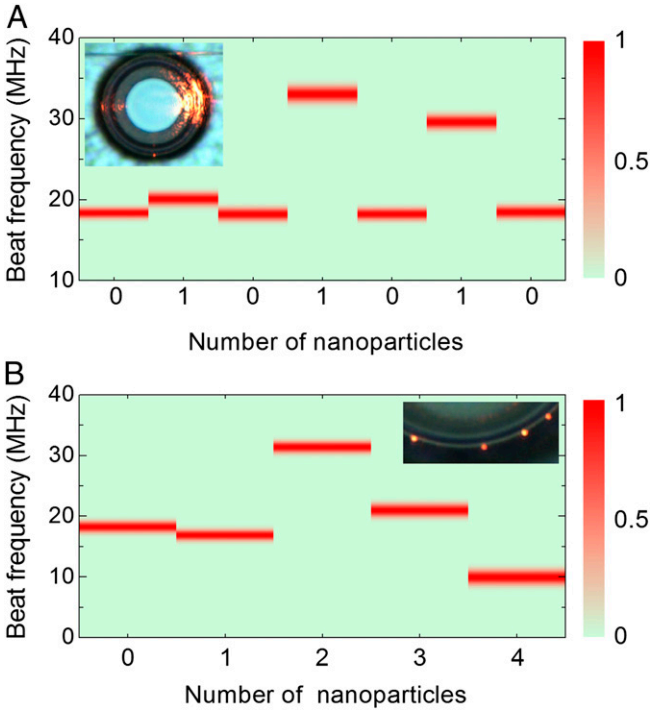

Fig. 4. Single nanoparticle detection in air. (*A*) The beat frequency change when a single PS nanoparticle with a radius of 50 nm is repeatedly transferred to and from the microcavity surface. (*B*) The beat frequency change when single nanoparticles are transferred to the cavity surface one by one. The widths of the data points represent the corresponding SDs of the beat frequencies. *Insets* are the optical micrographs showing one (*A*) and four (*B*) nanoparticles bound to the cavity surface.

Real-Time Single Nanoparticle Detection in an Aqueous Environment. To further study the performance of the Raman-lasing sensor, in the following, we perform real-time single nanoparticle detection in an aqueous environment. We first immerse the taper-microcavity coupling system into a chamber filled with pure water and record both the Raman spectrum and the Raman power in the time domain. To maintain ultra-high Q factors and thus enable Raman lasing in water, we use microspheres instead of microtoroids to avoid the cavity surface contamination originating from the silicon chip. To reduce the radiation loss of the cavity mode field in the aqueous environment, a microsphere with a diameter of ~90 μm (the corresponding mode volume of the fundamental mode is ~800 μm^3) is used, which has a Q factor of 1×10^8 in the 680-nm band in pure water. The largest mode function is ~0.15 at the surface, with the mode function defined as $f^2(x) = |E(x)|^2 / \max[|E|^2]$, where $|E(x)|^2$ and $\max[|E|^2]$ denote the field intensity at position x and the maximum field intensity, respectively. Using 2-mW pump power, Raman lasing is observed up to the second order in pure water, as shown in Fig. 5*A*. The temporal stability of the beat frequency of the first-order Raman laser in pure water is tested, by continuously recording the beat frequency for 30 s, with the result shown in Fig. 5*B*. The intrinsic beat frequency is ~8.16 MHz, with a temporal SD of ~277 kHz for 30 s.

We then inject the solution containing PS nanoparticles with a radius $r = 40$ nm and a concentration of ~5 pM into the chamber and measure the beat frequency change. As shown in Fig. 5*C*, abrupt changes in the beat frequency are observed, corresponding to single nanoparticle binding events. Upward and

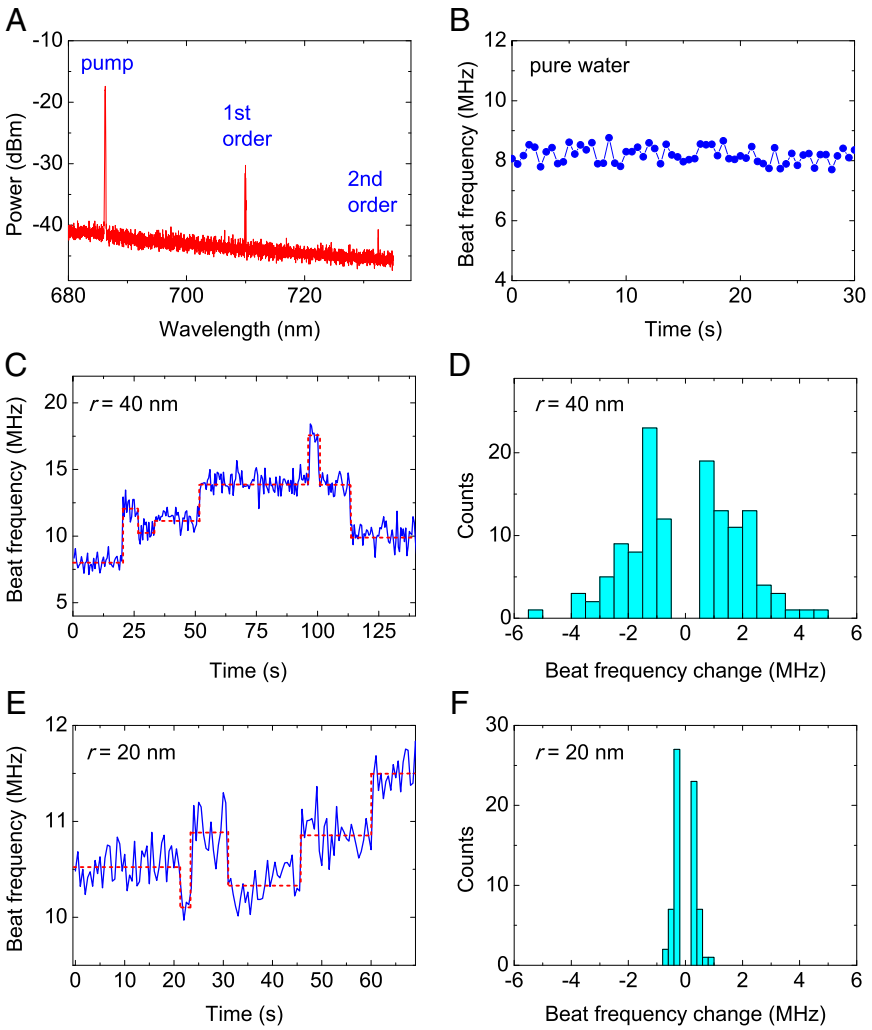

Fig. 5. Real-time single nanoparticle detection in an aqueous environment. (*A*) The Raman spectrum of the microcavity in pure water with a pump power of ~2 mW. (*B*) The beat frequency of the first-order Raman laser as a function of time, which is continuously measured for 30 s when the microcavity is immersed in pure water. The intrinsic beat frequency of the microcavity Raman laser is ~8.16 MHz, with an SD of ~277 kHz. (*C*) The beat frequency change as a function of time after the injection of the solution containing PS nanoparticles with a radius of 40 nm into the chamber. (*D*) Histogram showing the distribution of the discrete changes in beat frequency induced by 40-nm nanoparticles. (*E*) The beat frequency change vs. time when the chamber is filled with the solution containing PS nanoparticles with a radius of 20 nm. (*F*) Histogram showing the distribution of the discrete changes in beat frequency induced by 20-nm nanoparticles. The red dashed lines in *C* and *E* are drawn at the average beat frequency for each single nanoparticle binding event.

downward steps are both observed, and the distribution of the step changes in the beat frequency is plotted in Fig. 5*D*. To push this sensing method to its limit in an aqueous environment, we finally repeat the experiment with 20-nm-radius PS nanoparticles, with the result plotted in Fig. 5*E*. Discrete changes in the beat frequency are also observed, with the distribution plotted in Fig. 5*F*. From Fig. 5 *D* and *F*, we can see that the step changes in beat frequency are typically larger for 40-nm-radius nanoparticles than 20-nm-radius nanoparticles.

Discussion

Suppression of Cavity Optomechanical Oscillations. In high Q microcavities, optomechanical oscillations can also be excited, competing with stimulated Raman scattering. Note that the cavity size variations induced by optomechanical oscillations shift the resonance frequencies of both the pump and Raman modes, thus leading to similar oscillations of the Raman power, even without mode splitting (43). Optomechanical oscillations unfortunately have frequencies of the same order of magnitude as the beat note produced by mode splitting (several tens of megahertz), making it difficult to distinguish between the two. To eliminate the optomechanically induced oscillations in the Raman power, in the nanoparticle detection experiment in air, we use microtoroids with very thick silicon pillars. As shown in the *Inset* of Fig. 4*A*, the distance between the silicon pillar and the silica ring is controlled to be smaller than 10 μm, which can effectively suppress optomechanical oscillations without affecting the thresholds of the Raman lasers. As for detection in an aqueous environment, the mechanical oscillations are intrinsically suppressed because water increases the damping of the oscillations.

Detection Limit of the Microcavity Raman Lasing Sensor. We now discuss the detection limit of this Raman lasing sensor, which can be estimated from the condition that the Raman beat frequency changes be greater than the detection noise. For simplicity, we consider a cavity without intrinsic backscattering. In this case, the beat frequency of the Raman laser induced by the first nanoparticle is $2g = \alpha f^2(x)\omega_R/V_m$, where $f^2(x)$, ω_R, and V_m denote the mode function at the cavity surface, resonance frequency, and the mode volume of the Raman cavity mode, respectively.

$\alpha = 4\pi r^3(\varepsilon_p - \varepsilon_m)/(\varepsilon_p + 2\varepsilon_m)$ is the polarizability of the nanoparticle, with r being the radius of the particle, and ε_p and ε_m being the relative permitivities of the nanoparticle ($\varepsilon_p = 1.59^2$ for a PS particle) and surrounding medium ($\varepsilon_m = 1.33^2$ for water, and $\varepsilon_m = 1^2$ for air), respectively. Using the experimental parameters in the aqueous environment, the maximum beat frequency induced by a single 40-nm-radius nanoparticle and a 20-nm-radius nanoparticle are calculated to be ~ 8 and ~ 1 MHz, respectively, which agree well with the largest values in our experiment (Fig. 5 *D* and *F*). The detection limit is then estimated from the noise level of the beat frequency. In the aqueous environment, the typical detection noise of the beat frequency is ~ 277 kHz. Taking the experimental parameters, $\omega_R = 2\pi \times 4.24 \times 10^{14}$ Hz, a spherical cavity diameter of ~ 90 μm (corresponding $V_m \sim 800$ μm^3), and a mode function $f^2(x) \sim 0.15$ at the cavity surface, the smallest detectable nanoparticle in an aqueous environment is estimated to be ~ 14 nm in radius. In air, the detection limit can be further improved because of the larger refraction index contrast between the target particle and the surrounding medium.

The detection noise of the Raman beat frequency originates mainly from the uncertainty of choosing the center part of each envelope of the beat oscillations, instead of the fundamental line width of the Raman laser, which is generally at the level of several Hertz (44). Experimentally, the detection noise can be suppressed by optimizing the parameters. For instance, by increasing the pump power, more envelopes of beat oscillations can be generated, and the detection noise of the Raman beat frequency can thus be decreased through averaging over all of the beat frequencies in each envelope. By doing this, we experimentally decreased the noise level of the Raman beat frequency to ~ 190 kHz in an aqueous environment (for details, see Fig. S2). In addition, by appropriately locking the frequency of the excitation light to that of the pump cavity mode (45), a stable beat oscillation of the Raman lasers may be observed, which should have smaller beat frequency measurement noise. Furthermore, an even lower detection limit may be reached by using plasmonic enhancement (46–51).

Conclusion

In conclusion, we realized, for the first time to our knowledge, ultrasensitive nanoparticle detection using split-mode microcavity Raman lasers. The sensing mechanism is first demonstrated in air, by controllably transferring single nanoparticles with a radius of 50 nm to the cavity surface. By monitoring the abrupt change in beat frequency of the microcavity Raman laser, we then realize real-time detection of single nanoparticles in an aqueous environment, with a record low detection limit of 20 nm in radius, without using any additional techniques to suppress the laser frequency noise. Benefiting from the nature of Raman lasers, this split-mode microcavity Raman lasing sensor provides a practical sensing platform with high sensitivity.

Methods

For nanoparticle detection in air, we use the nanoparticle transfer technique introduced in ref. 19. We first immerse a fiber taper into a solution containing PS nanoparticles and then take it out. After this process, many nanoparticles are bound to the taper surface. A single nanoparticle can be transferred from the fiber taper to the microcavity surface, or vice versa, by contacting the fiber to the microcavity. A new fiber taper is used for exciting WGMs in the microcavity. In the experiment, we either repeatedly transfer a single nanoparticle between the fiber taper and the microcavity surface or transfer the nanoparticles one by one to the microcavity surface and measure the beat frequency change after every nanoparticle transfer, in the same manner as shown in Fig. 4. During the nanoparticle transfer, a microscope is used to monitor the process with the pump laser in the visible wavelength, thus making it possible to directly observe the nanoparticles with a microscope due to light scattering off them, as shown in the *Insets* of Fig. 4 *A* and 4*B*.

ACKNOWLEDGMENTS. This work was supported by 973 Program Grant 2013CB328704; National Science Foundation of China Grants 11474011, 11222440, 11121091, and 61435001; and Beijing Natural Science Foundation Program Grant 4132058.

1. Freudiger CW, et al. (2008) Label-free biomedical imaging with high sensitivity by stimulated Raman scattering microscopy. *Science* 322(5909):1857–1861.
2. Min B, Kippenberg TJ, Vahala KJ (2003) Compact, fiber-compatible, cascaded Raman laser. *Opt Lett* 28(17):1507–1509.
3. Shverdin MY, Walker DR, Yavuz DD, Yin GY, Harris SE (2005) Generation of a single-cycle optical pulse. *Phys Rev Lett* 94(3):033904.
4. Vahala KJ (2003) Optical microcavities. *Nature* 424(6950):839–846.
5. Qian S-X, Chang RK (1986) Multiorder stokes emission from micrometer-size droplets. *Phys Rev Lett* 56(9):926–929.
6. Lin HB, Campillo AJ (1994) cw nonlinear optics in droplet microcavities diplaying enhanced gain. *Phys Rev Lett* 73(18):2440–2443.
7. Spillane SM, Kippenberg TJ, Vahala KJ (2002) Ultralow-threshold Raman laser using a spherical dielectric microcavity. *Nature* 415(6872):621–623.
8. Kippenberg TJ, Spillane SM, Armani DK, Vahala KJ (2004) Ultralow-threshold microcavity Raman laser on a microelectronic chip. *Opt Lett* 29(11):1224–1226.
9. Yang L, Carmon T, Min B, Spillane SM, Vahala KJ (2005) Erbium-doped and Raman microlasers on a silicon chip fabricated by the sol-gel process. *Appl Phys Lett* 86(9): 091114.
10. Grudinin IS, Maleki L (2007) Ultralow-threshold Raman lasing with CaF2 resonators. *Opt Lett* 32(2):166–168.
11. Li B-B, Xiao Y-F, Yan M-Y, Clements WR, Gong Q (2013) Low-threshold Raman laser from an on-chip, high-Q, polymer-coated microcavity. *Opt Lett* 38(11):1802–1804.
12. Chistiakova MV, Armani AM (2012) Cascaded Raman microlaser in air and buffer. *Opt Lett* 37(19):4068–4070.
13. Bixler JN, et al. (2014) Ultrasensitive detection of waste products in water using fluorescence emission cavity-enhanced spectroscopy. *Proc Natl Acad Sci USA* 111(20): 7208–7211.
14. Weiss DS, et al. (1995) Splitting of high-Q Mie modes induced by light backscattering in silica microspheres. *Opt Lett* 20(18):1835–1837.
15. Mazzei A, et al. (2007) Controlled coupling of counterpropagating whispering-gallery modes by a single Rayleigh scatterer: A classical problem in a quantum optical light. *Phys Rev Lett* 99(17):173603.
16. Teraoka I, Arnold S (2009) Resonance shifts of counterpropagating whispering-gallery modes: Degenerate perturbation theory and application to resonator sensors with axial symmetry. *J Opt Soc A B* 26(7):1321–1329.
17. Yi X, et al. (2011) Multiple-Rayleigh-scatterer-induced mode splitting in a high-Q whispering-gallery-mode microresonator. *Phys Rev A* 83(2):023803.
18. Zhu J, et al. (2010) On-chip single nanoparticle detection and sizing by mode splitting in an ultrahigh-Q microresonator. *Nat Photonics* 4(1):46–49.
19. Shao L, et al. (2013) Detection of single nanoparticles and lentiviruses using microcavity resonance broadening. *Adv Mater* 25(39):5616–5620.
20. Vollmer F, et al. (2002) Protein detection by optical shift of a resonant microcavity. *Appl Phys Lett* 80(21):4057–4059.
21. Arnold S, Khoshsima M, Teraoka I, Holler S, Vollmer F (2003) Shift of whispering-gallery modes in microspheres by protein adsorption. *Opt Lett* 28(4):272–274.
22. Vollmer F, Arnold S (2008) Whispering-gallery-mode biosensing: Label-free detection down to single molecules. *Nat Methods* 5(7):591–596.
23. Vollmer F, Arnold S, Keng D (2008) Single virus detection from the reactive shift of a whispering-gallery mode. *Proc Natl Acad Sci USA* 105(52):20701–20704.
24. Arnold S, Shopova SI, Holler S (2010) Whispering gallery mode bio-sensor for label-free detection of single molecules: Thermo-optic vs. reactive mechanism. *Opt Express* 18(1):281–287.
25. Shopova SI, Rajmangal R, Nishida Y, Arnold S (2010) Ultrasensitive nanoparticle detection using a portable whispering gallery mode biosensor driven by a periodically poled lithium-niobate frequency doubled distributed feedback laser. *Rev Sci Instrum* 81(10):103110.
26. Li H, Guo Y, Sun Y, Reddy K, Fan X (2010) Analysis of single nanoparticle detection by using 3-dimensionally confined optofluidic ring resonators. *Opt Express* 18(24):25081–25088.
27. Lu T, et al. (2011) High sensitivity nanoparticle detection using optical microcavities. *Proc Natl Acad Sci USA* 108(15):5976–5979.
28. Swaim JD, Knittel J, Bowen WP (2013) Detection of nanoparticles with a frequency locked whispering gallery mode microresonator. *Appl Phys Lett* 102(18):183106.
29. Knittel J, Swaim JD, McAuslan DL, Brawley GA, Bowen WP (2013) Back-scatter based whispering gallery mode sensing. *Sci Rep* 3:2974.
30. Yang J, Guo LJ (2006) Optical sensors based on active microcavities. *IEEE J Sel Top Quantum Electron* 12(1):143–147.
31. Kim W, Ozdemir SK, Zhu J, He L, Yang L (2010) Demonstration of mode splitting in an optical microcavity in aqueous environment. *Appl Phys Lett* 97(7):071111.
32. Zhu J, Özdemir SK, He L, Yang L (2010) Controlled manipulation of mode splitting in an optical microcavity by two Rayleigh scatterers. *Opt Express* 18(23):23535–23543.
33. Zhu J, Özdemir SK, He L, Chen DR, Yang L (2011) Single virus and nanoparticle size spectrometry by whispering-gallery-mode microcavities. *Opt Express* 19(17):16195–16206.
34. Kim W, Ozdemir SK, Zhu J, Yang L (2011) Observation and characterization of mode splitting in microsphere resonators in aquatic environment. *Appl Phys Lett* 98(14): 141106.

35. He L, Ozdemir SK, Zhu J, Yang L (2010) Ultrasensitive detection of mode splitting in active optical microcavities. *Phys Rev A* 82(5):053810.
36. He L, Ozdemir SK, Zhu J, Kim W, Yang L (2011) Detecting single viruses and nanoparticles using whispering gallery microlasers. *Nat Nanotechnol* 6(7):428–432.
37. Maker AJ, Armani AM (2013) Heterodyned toroidal microlaser sensor. *Appl Phys Lett* 103(12):123302.
38. Armani DK, Kippenberg TJ, Spillane SM, Vahala KJ (2003) Ultra-high-Q toroid microcavity on a chip. *Nature* 421(6926):925–928.
39. Knight JC, Cheung G, Jacques F, Birks TA (1997) Phase-matched excitation of whispering-gallery-mode resonances by a fiber taper. *Opt Lett* 22(15):1129–1131.
40. Kippenberg TJ, Spillane SA, Min B, Vahala KJ (2004) Theoretical and experimental study of stimulated and cascaded Raman scattering in ultrahigh-Q optical microcavities. *IEEE J Sel Top Quantum Electron* 10(5):1219–1228.
41. Carmon T, Yang L, Vahala K (2004) Dynamical thermal behavior and thermal self-stability of microcavities. *Opt Express* 12(20):4742–4750.
42. Wiersig J (2011) Structure of whispering-gallery modes in optical microdisks perturbed by nanoparticles. *Phys Rev A* 84(6):063828.
43. Carmon T, Rokhsari H, Yang L, Kippenberg TJ, Vahala KJ (2005) Temporal behavior of radiation-pressure-induced vibrations of an optical microcavity phonon mode. *Phys Rev Lett* 94(22):223902.
44. Lu T, Yang L, Carmon T, Min B (2011) A narrow-linewidth on-chip toroid Raman laser. *IEEE J Quantum Electron* 47(3):320–326.
45. Brasseur JK, Teehan R, Knize RJ, Roos PA, Carlsten JL (2001) Phase and frequency stabilization of a pump laser to a Raman active resonator. *IEEE J Quantum Electron* 37(8):1075–1083.
46. Shopova SI, Rajmangal R, Holler S, Arnold S (2011) Plasmonic enhancement of a whispering-gallery-mode biosensor for single nanoparticle detection. *Appl Phys Lett* 98(24):243104.
47. Santiago-Cordoba MA, Boriskina SV, Vollmer F, Demirel MC (2011) Nanoparticle-based protein detection by optical shift of a resonant microcavity. *Appl Phys Lett* 99(7):073701.
48. Swaim JD, Knittel J, Bowen WP (2011) Detection limits in whispering gallery biosensors with plasmonic enhancement. *Appl Phys Lett* 99(24):243109.
49. Xiao Y-F, et al. (2012) Strongly enhanced light-matter interaction in a hybrid photonic-plasmonic resonator. *Phys Rev A* 85(3):031805.
50. Dantham VR, Holler S, Kolchenko V, Wan Z, Arnold S (2012) Taking whispering gallery-mode single virus detection and sizing to the limit. *Appl Phys Lett* 101(4):043704.
51. Dantham VR, et al. (2013) Label-free detection of single protein using a nanoplasmonic-photonic hybrid microcavity. *Nano Lett* 13(7):3347–3351.